ChemComm

COMMUNICATION

View Article Online
View Journal

CrossMark click for updates

Cite this: DOI: 10.1039/c4cc10203g

Received 21st December 2014,
Accepted 20th January 2015

DOI: 10.1039/c4cc10203g

www.rsc.org/chemcomm

Ultra-small nanoparticles of $MgTi_2O_5$ embedded in carbon rods with superior rate performance for sodium ion batteries†

Fangxi Xie,[a] Yuanfu Deng,*[bc] Ye Xie,[b] Hongjie Xu[d] and Guohua Chen*[acd]

Confinement of ultra-small $MgTi_2O_5$ nanoparticles in carbon is demonstrated to be an efficient method for fabricating long cycle-life anode material for sodium ion batteries. Superior rate and excellent cyclic capabilities as well as high Coulombic efficiency of the $MgTi_2O_5$–C nanocomposite, obtained from pyrolysis of a single molecule precursor, are shown.

Lithium ion batteries (LIBs) are considered one of the most mature candidates for the electrification of transportation and renewable energy integration due to their long lifetime, high energy density and low environmental impact.[1,2] However, there is increasing attention on the cost and the limited lithium supply for large-scale energy storage applications. Therefore, sodium ion batteries (SIBs), new low-cost and reliable electrochemical energy storage devices, have attracted significant attention because of the abundant supply of sodium.[3–6] It is known that the properties of the SIBs are mostly determined by the performance of the active electrode materials. Thus, investigations on the novel materials with good electrochemical performance are very significant and in urgent demand. Compared with the fast development of the cathode materials,[7–9] only some of the Na-storage anode materials have reported to demonstrate certain redox capacity and adequate duration.[5,6] Up to now, amorphous phosphorus, metal phosphides, hard carbon, and alloys have been successfully tested as anode materials for SIBs.[10–19] Among these materials, amorphous P–C composites, metal phosphides and alloys exhibit high specific capacities. These composites however would not be suitable for long-life batteries owing to the large volume change during sodium insertion and extraction. Hard carbon shows a high specific capacity and good cycling performance.[20,21] However, most of the capacity is located at the voltage below 0.1 V, which is near zero *versus* Na^+/Na, causing potential safety concerns, especially at a fast charging rate or overcharging.[22,23] Besides the materials mentioned above, Ti-based oxides have attracted much attention because of their low price, environmental friendliness, good cycling performance and, most importantly, high safety, which is derived from the high sodium insertion voltage, for example, 0.91 V for the spinel $Li_4Ti_5O_{12}$.[23] The spinel $Li_4Ti_5O_{12}$, a "zero-strain" anode material for the LIBs, was recently investigated as anode material for SIBs.[23,24] Nanorod anatase TiO_2 with the carbon layers also shows excellent cyclability and high-rate capability in the insertion and extraction process of Na^+.[25] Recent studies suggested that the electrochemical performance of the Ti-based oxides can be optimized by shortening the diffusion path of sodium ions and improvement of the conductivity.[25–27] It is noted that reducing the particle size of anode materials to the nanoscale (especially < 10 nm) can endure much higher strain and effectively mitigate pulverization.[25] However, nano-sized particles tend to aggregate during the cycles, resulting in a fast capacity decay. Correspondingly, integrating nanomaterial with a conductive matrix such as carbon can decrease the opportunities for particle aggregation and accommodate volume expansion for keeping the integrity of the electrode.[28] From the points of view of high specific capacity and high conductivity of hard carbon material and the safety of the Ti-based oxides, novel Ti-based oxides–carbon nanocomposites with ultra-small particle sizes should be desirable anode materials for SIBs.

Herein, a novel hybrid $MgTi_2O_5$–C (MTO–C) nanocomposite is reported, for the first time, as a superior anode material for SIBs. The $MgTi_2O_5$–C nanocomposite in the nanorod shape, consisting of ultra-small $MgTi_2O_5$ nanoparticles (NPs) embedded by evenly distributed carbon, was firstly prepared from an *in situ* carbonization process of a cheap single molecule precursor with unique morphology. Such $MgTi_2O_5$–C nanocomposites with porous structure and ultra-small particle size are designed with four specific aims in mind: (1) enhancement of the conductivity of $MgTi_2O_5$ for

[a] *Centre for Green Products and Processing Technologies, Fok Ying Tung Graduate School, The Hong Kong University of Science and Technology, Clear Water Bay, Hong Kong, P. R. China*
[b] *The Key Laboratory of Fuel Cell Technology of Guangdong Province, School of Chemistry and Chemical Engineering, South China University of Technology, Guangzhou, 510640, China. E-mail: chyfdeng@scut.edu.cn*
[c] *Centre for Green Products and Processing Technologies, Guangzhou HKUST Fok Ying Tung Research Institute, Guangzhou, 511458, China*
[d] *Department of Chemical and Biomolecular Engineering, The Hong Kong University of Science and Technology, Clear Water Bay, Hong Kong, P. R. China. E-mail: kechengh@ust.hk*

† Electronic supplementary information (ESI) available. See DOI: 10.1039/c4cc10203g

facilitating good transport of electrons from the poorly conducting $MgTi_2O_5$; (2) utilization of the high specific capacity of the hard carbon to increase the specific capacity of the composite; (3) decrease in the capacity over the range of 0–0.1 V to improve the safety of the anode material; and (4) preservation of fast transport of sodium ions by shortening their diffusion path and prevention of the aggregation of $MgTi_2O_5$ nanoparticles. The facile, simple and cost-effective route using a single source precursor could be extended to the preparation of other high performance electrode materials.

Two steps are involved in the typical preparation of the $MgTi_2O_5$–C composite: the PVP-assisted (PVP = Polyvinylpyrrolidone) crystallization process of a single molecule precursor $(NH_4)_2Mg(H_2O)_6[Ti(C_6H_6O_7)_3]_2{\cdot}6H_2O$ and the calcination of the precursor.[29] The detailed procedure can be found in the experimental section. The samples obtained from pyrolysis of the precursor at 600 °C in Ar and air are named MTO-Ar or MTO-Air, respectively.

Fig. 1 shows the X-ray diffraction (XRD) patterns of the as-prepared MTO-Ar, MTO-Air, and the standard $MgTi_2O_5$ (JCPDS Card No. 35-0792). All of the peaks of MTO-Air can be readily indexed to crystalline $MgTi_2O_5$. However, there are no obvious peaks found in the XRD pattern of the MTO-Ar sample, which may be attributed to the ultra-small size of $MgTi_2O_5$ particles obtained. And the detailed analysis of XRD (Fig. S1, ESI†) revealed the existence of crystalline $MgTi_2O_5$. To determine whether any impurities, which cannot be detected by XRD, are present in the as-prepared MTO-Ar sample, XRD data were collected on the annealed MTO-Ar (500 °C in air for 1 h). If there is any impurity, then the impurity will crystallize during annealing and then be detected by XRD. As shown in Fig. 1, no obvious impurity peaks of TiO_2, $MgTiO_3$ or MgO appeared on the annealed sample with all the peaks matching with the standard $MgTi_2O_5$, suggesting that the as-prepared MTO-Ar sample has no impurity except for amorphous carbon. A similar method for the characterization of ultra-small $Li_4Ti_5O_{12}$ nanoparticles has been reported previously.[30] The presence of pure $MgTi_2O_5$ and amorphous carbon in the MTO-Ar sample is also supported by the Raman spectrum of the MTO-Ar sample (Fig. S2a, ESI†), in which the peaks between 100 to 1000 cm^{-1} are in agreement with the Raman signals of pure $MgTi_2O_5$.[31] The two peaks at 1335 and 1580 cm^{-1} can be assigned to the typical D and G bands of amorphous carbon, respectively.[32] 26.0 wt% of carbon in the MTO-Ar sample was determined from TG analysis (as shown in Fig. S3, ESI†).

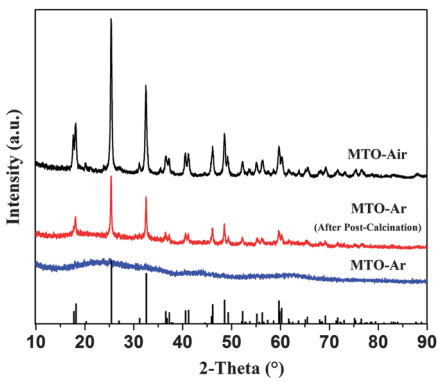

Fig. 1 The representative X-ray diffraction (XRD) patterns of different materials.

The morphology of the as-prepared $MgTi_2O_5$–C composite was characterized using scanning electron microscopy (SEM) and transmission electron microscopy (TEM) images. As shown in Fig. 2(A), the shape of the composite is rod-like with smooth surface and various diameters from several micrometers to tens of micrometers, similar to the shape of the precursor (Fig. S4, ESI†). The high resolution SEM image (Fig. 2(B)) shows that the MTO-Ar sample is of woody appearance with some ultra-small nanoparticles attached to the surface. The $MgTi_2O_5$ NPs (black dots) with a uniform particle size were homogenously embedded in the carbon framework (Fig. 2(C)). The typical size of $MgTi_2O_5$ particles is around 5 nm, which could also be clearly seen from the high resolution TEM (HRTEM) image (Fig. 2(D)). The lattice fringes are visible (Fig. 2(D)), with a *d*-spacing of 0.49 nm, corresponding to the (200) plane of $MgTi_2O_5$. This is also direct proof of the existence of $MgTi_2O_5$ nanoparticles in the MTO-Ar sample. The energy dispersive spectrometer (EDS) mapping (Fig. 2(E)) of the selection region (Fig. S5, ESI†) of the as-prepared sample demonstrates that $MgTi_2O_5$ NPs are highly dispersed in the carbon matrix.

The unique morphology and structure of the as-prepared $MgTi_2O_5$–C composite motivate us to further investigate its electrochemical performance. For comparison, the pure $MgTi_2O_5$ (MTO-Air) obtained from the calcination of the precursor in air at 600 °C with a particle size of ~30 nm (Fig. S6, ESI†) was also investigated. Fig. 3(A) shows the typical cyclic voltammograms (CVs) of the $MgTi_2O_5$–C electrode for the initial three cycles at a scan rate of

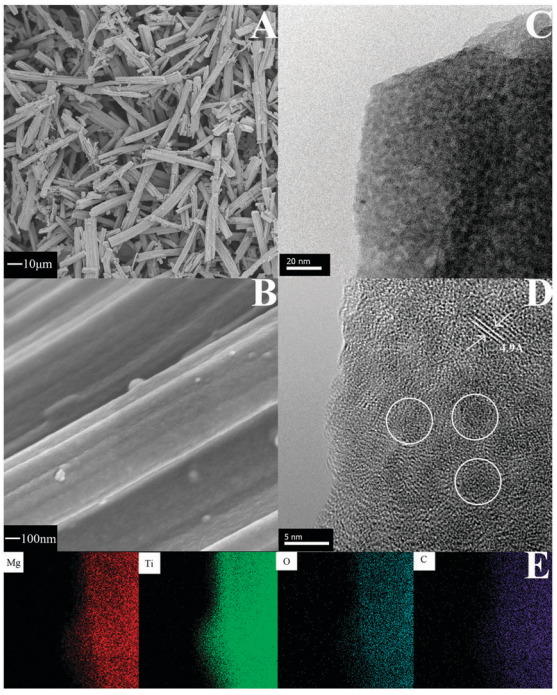

Fig. 2 (A) Low Magnification SEM image of MTO-Ar; (B) high magnification SEM image of MTO-Ar; (C) TEM image of MTO-Ar; (D) HRTEM image of MTO-Ar and (E) the elemental mapping of the transmission electron microscope image of MTO-Ar.

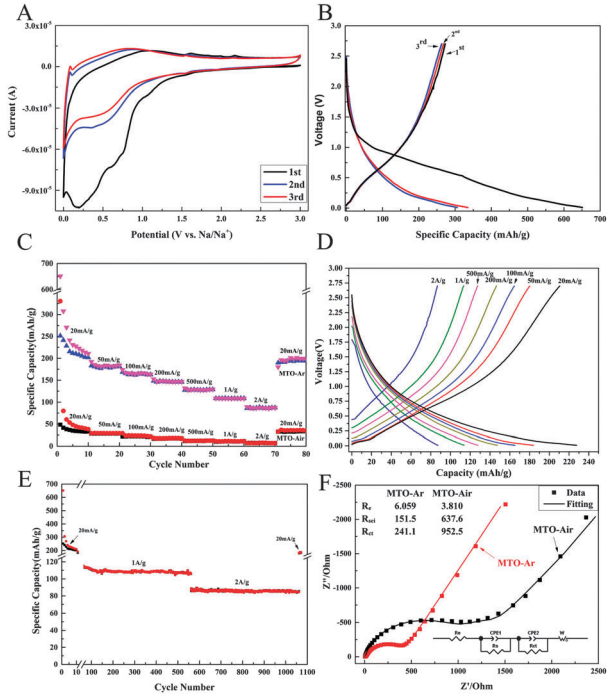

Fig. 3 (A) Cyclic voltammetry curves of MTO-Ar for SIBs; (B) initial cycle curves of MTO-Ar for SIBs; (C) the comparison of specific capacities of MTO-Ar and MTO-Air under different current densities for SIBs; (D) the typical cycle curves of MTO-Ar under different current densities for SIBs; (E) the long cycle performance of MTO-Ar for SIBs under selected current densities and (F) comparison of the Nyquist plots of MTO-Ar and MTO-Air electrodes for SIBs.

0.1 mV s^{-1} between 0 and 3.0 V. During the first cathodic sweep, there are three main reduction peak regions located at around 1.1, 0.8 to 0.2 and 0.2 to 0.01 V, respectively. For the reduction peak at around 1.1 V, it can be assigned to the reaction between the Na ion and the surface functional group of carbon.[33] The broad reduction peak at 0.8 to 0.2 V is mainly ascribed to the decomposition of the electrolyte to form solid-electrolyte interphase (SEI) film and the reduction peak of $Ti^{4+/3+}$,[34,35] which could also be found in the CVs (Fig. S7, ESI†) of the MTO-Air and the other two $MgTi_2O_5$–C samples (MTO-Ar-PC-2h and MTO-Ar-PC-12h). The two samples with 1.0 and 3.0% carbon content (Fig. S8, ESI†) and ultra-small $MgTi_2O_5$ nanoparticles (Fig. S9, ESI†) were respectively obtained from post-calcination of MTO-Ar under Ar with 5% O_2 for 2 and 12 h. The initial abrupt mass reduction of these samples in the TGA curves at around 100–250 °C comes from the adsorbed water and gases, which agrees with the endothermal peaks of MTO-Ar in this area and the difference in the mass amount might come from the different amount of adsorbed water and gases.[36] The sharp reduction peaks appearing in the low potential region from 0.01 to 0.2 V can be attributed to the insertion of Na ions in carbon.[32] During the anodic sweep, two main oxidation peak regions located at 0.01 to 0.2 and 0.2 to 1.2 V are observed, which should be attributed to the removal of Na ions from the carbon and $MgTi_2O_5$, respectively.[25,33,34] However, the absence of these peaks in the CV curves of MTO-Air implies the large irreversible capacity of the initial cycle of MTO-Air. The intensity of the CV peaks decreases over the first few cycles, indicating some capacity fading during the initial cycling. Fig. 3(B) shows the representative discharge–charge profiles of the $MgTi_2O_5$–C electrode for the 1st, 2nd and 3rd cycles at a current density of 20 mA g^{-1} between the cut-off potentials of 0.01 to 2.7 V. All the specific capacity reported here is calculated on the basis of the total mass of the $MgTi_2O_5$–C composite. The first discharge and charge capacities of $MgTi_2O_5$–C are 651.5 and 251.5 mA h g^{-1}, respectively, corresponding to a Coulombic efficiency (CE) of 38.6%, which is similar to the previous reported literature on hard carbon[33,37] and carbon-coated TiO_2 anode materials.[25] The low initial CE can be mainly attributed to the formation of SEI film by reduction of the electrolyte on the surface of material[33,37] and/or irreversible sodium insertion into special sites[35] during the first discharge process. This low initial CE might cause the reduction of the energy density of a full sodium ion battery.[38]

It is noted that the specific charge capacity below 2.0 V, the practically useful part of the full cell, comprises ~85% of the whole de-insertion capacity. In addition, the specific discharge capacity below 0.1 V is only ~10% of the whole insertion capacity, which is much smaller than that of the hard carbon in the reported literature.[21,33,37] This is important for the safety of the practical application in SIBs. Fig. 3(C) shows the rate performance of MTO-Ar and MTO-Air electrodes cycled at various current densities from 20 to 2000 mA g^{-1}. The corresponding discharge–charge curves of MTO-Ar electrode are given in Fig. 3(D). It is clearly seen that the MTO-Ar electrode exhibits a much better rate performance than that of the MTO-Air electrode. MTO-Ar displays a respective specific capacity of 200, 180, 165, 146, 128, 109 and 86 mA h g^{-1} at 20, 50, 100, 200, 500, 1000 and 2000 mA g^{-1}. However, only a small capacity of 25 mA h g^{-1} was obtained from the MTO-Air sample at 50 mA g^{-1}. It should be pointed out that the rate capability obtained from the MTO-Ar sample can be comparable to the carbon-coated anatase,[25] a novel anode material for SIBs, and the state-of-the-art hard carbon-based anode materials.[21,32,35] In addition, the rate performance of the MTO-Ar is much better than the carbon anode obtained from the pyrolysis of $(NH_4)_3Hcit$, although the carbon anode has the same specific capacity of MTO-Ar at low current density (Fig. S10, ESI†). The superior rate capability of MTO-Ar should be related to the beneficial combination of the high electric conductivity offered by the carbon matrix and the short diffusion path for both electrons and ions provided by the ultra-small $MgTi_2O_5$ particles. Besides, the specific capacity resumes to 200 mA h g^{-1} when the discharge–charge current density is lowered to 20 mA g^{-1}, indicating that the unique structure of the $MgTi_2O_5$–C composite could preserve the integrity of the electrode and thus is tolerant to the varied charge and discharge currents, which is another critical property for practical power applications in SIBs. To evaluate the cycling performance of this novel hybrid material as the anode material for SIBs, the electrode was cycled for more than 1000 cycles under different current densities. Fig. 3(E) displays the cyclability of the MTO-Ar electrode after the tests of the rate performance in the first 80 cycles, then 1000 mA g^{-1} for the subsequent 500 cycles, 2000 mA g^{-1} for another 500 cycles and 20 mA g^{-1} for the final 10 cycles. Importantly, this novel hybrid structure of $MgTi_2O_5$–C shows a very impressive cycling performance. When cycled at 1000 mA g^{-1}, the MTO-Ar exhibits an initial capacity of 113 mA h g^{-1}, with high

capacity retention of 92% after even 500 cycles. When cycled at 2000 mA g^{-1}, it shows an initial capacity of 85 mA h g^{-1}, with high capacity retention of 98% after 500 cycles. When the current density is decreased to 20 mA g^{-1}, a capacity of 200 mA h g^{-1} can also be obtained with almost no capacity decrease observed in the following 10 cycles. During cycling, the CE of >99% was achieved after the first several cycles, also demonstrating the good reversibility for sodium storage capability of the $MgTi_2O_5$–C electrode. Fig. 3(F) displays the impedance spectra of the primary MTO-Air and MTO-Ar electrodes. The Nyquist plots can be fitted to and interpreted well with the equivalent electric circuit (as shown in the inset of Fig. 3(F)). The resistance (R_s) of the solid electrolyte interface (SEI) and the resistance of charge transfer of (R_{ct}) MTO-Ar are significantly lower than those of MTO-Air, which could be attributed to the smaller size and the presence of the carbon matrix. The low resistances of the MTO-Ar electrode result in the superior rate performance and cycling stability. Consequently, the high capacity, the good cyclability and rate performance of the MTO-Ar composite could be attributed to the following several merits. First, carbon with good conductivity can provide some specific capacity as an additional anode material and also provide good electric conductivity. Second, the presence of carbon in the composite could significantly relax the strain generated during the sodiation–desodiation processes and then suppress the aggregation and fracture of $MgTi_2O_5$ nanoparticles. Finally, the extraordinary small size of $MgTi_2O_5$ nanoparticles could provide the short diffusion path for both electrons and sodium ions.

In order to study the effects of particle size and carbon content on the reversibility of Na^+ intercalation process. The electrochemical performances of the MTO-Ar-PC-2h and MTO-Ar-PC-12h were also studied by discharge–charge process (Fig. S10, ESI†). Both of the samples display higher specific capacities than those of the MTO-Air at different current densities. But their capacities are both lower than those of MTO-Ar, especially at high discharge–charge current density. Furthermore, the MTO-Ar-PC-2h sample shows higher specific capacity and superior rate performance than those of the MTO-Ar-PC-12h sample because of its higher carbon content. These results demonstrate that the particle size and carbon have important synergistic roles in the improvement of the specific capacity and rate performance of the MTO-based anode material.

In conclusion, ultra-small nanoparticles of $MgTi_2O_5$ enwrapped in carbon nanorods as anode material for SIBs were successfully synthesized *via* the pyrolysis of a single molecule precursor for the first time. Excellent cycling performance with 98% capacity retention after 500 cycles under a current density of 2000 mA g^{-1} was obtained. This superior cycle and rate performance of the MTO-Ar electrode is believe to be derived from the good composition and excellent structure stability of the hybrid $MgTi_2O_5$–C composite, in which the homogenous distribution of the carbon matrix and ultra-small $MgTi_2O_5$ nanoparticles can prevent the aggregation and pulverization of the ultra-small particles during the discharge–charge processes.

This work was supported by the link project of Natural Science Foundation of China and Qinghai Province (U1407124), the Guangzhou Scientific and Technological Planning Project (2013J4100112, 2014J4500002) and the Fok Ying Tung Foundation (NRC07/08.EG01).

Notes and references

1 J. M. Tarascon and M. Armand, *Nature*, 2001, **414**, 359.
2 G. Jeong, Y. U. Kim, H. Kim, Y. J. Kim and H. J. Sohn, *Energy Environ. Sci.*, 2011, **4**, 1986.
3 V. Palomares, P. Serras, I. Villaluenga, K. B. Hueso, J. Carretero-Gonzalez and T. Rojo, *Energy Environ. Sci.*, 2012, **5**, 5884.
4 V. Palomares, M. Casas-Cabanas, E. Castillo-Martinez, M. H. Han and T. Rojo, *Energy Environ. Sci.*, 2013, **6**, 2312.
5 S. W. Kim, D. H. Seo, X. Ma, G. Ceder and K. Kang, *Adv. Energy Mater.*, 2012, **2**, 710.
6 H. Pan, Y. S. Hu and L. Chen, *Energy Environ. Sci.*, 2013, **6**, 2338.
7 K. H. Ha, S. H. Woo, D. Mok, N. S. Choi, Y. Park, S. M. Oh, Y. Kim, J. Kim, J. Lee, L. F. Nazar and K. T. Lee, *Adv. Energy Mater.*, 2013, **3**, 770.
8 K. Saravanan, C. W. Mason, A. Rudola, K. H. Wong and P. Balaya, *Adv. Energy Mater.*, 2013, **3**, 444.
9 Y. Cao, L. Xiao, W. Wang, D. Choi, Z. Nie, J. Yu, L. V. Saraf, Z. Yang and J. Liu, *Adv. Mater.*, 2011, **23**, 3155.
10 Y. Kim, Y. Park, A. Choi, N. S. Choi, J. Kim, J. Lee, J. H. Ryu, S. M. Oh and K. T. Lee, *Adv. Mater.*, 2013, **25**, 3045.
11 J. Qian, X. Wu, Y. Cao, X. Ai and H. Yang, *Angew. Chem., Int. Ed.*, 2013, **52**, 4633.
12 W. Li, S. L. Chou, J.-Z. Wang, J. H. Kim, H. K. Liu and S. X. Dou, *Adv. Mater.*, 2014, **26**, 4037.
13 J. Qian, Y. Xiong, Y. Cao, X. Ai and H. Yang, *Nano Lett.*, 2014, **14**, 1865.
14 K. Tang, L. Fu, R. J. White, L. Yu, M.-M. Titirici, M. Antonietti and J. Maier, *Adv. Energy Mater.*, 2012, **2**, 873.
15 Y. Cao, L. Xiao, M. L. Sushko, W. Wang, B. Schwenzer, J. Xiao, Z. Nie, L. V. Saraf, Z. Yang and J. Liu, *Nano Lett.*, 2012, **12**, 3783.
16 Y. Zhu, X. Han, Y. Xu, Y. Liu, S. Zheng, K. Xu, L. Hu and C. Wang, *ACS Nano*, 2013, **7**, 6378.
17 J. Qian, M. Zhou, Y. Cao, X. Ai and H. Yang, *Adv. Energy Mater.*, 2012, **2**, 410.
18 Y. Xu, Y. Zhu, Y. Liu and C. Wang, *Adv. Energy Mater.*, 2013, **3**, 128.
19 C. Zhu, X. Mu, P. A. van Aken, Y. Yu and J. Maier, *Angew. Chem., Int. Ed.*, 2014, **53**, 2152.
20 S. Komaba, W. Murata, T. Ishikawa, N. Yabuuchi, T. Ozeki, T. Nakayama, A. Ogata, K. Gotoh and K. Fujiwara, *Adv. Funct. Mater.*, 2011, **21**, 3859.
21 W. Luo, J. Schardt, C. Bommier, B. Wang, J. Razink, J. Simonsen and X. Ji, *J. Mater. Chem. A*, 2013, **1**, 10662.
22 K. Gotoh, T. Ishikawa, S. Shimadzu, N. Yabuuchi, S. Komaba, K. Takeda, A. Goto, K. Deguchi, S. Ohki, K. Hashi, T. Shimizu and H. Ishida, *J. Power Sources*, 2013, **225**, 137.
23 Y. Sun, L. Zhao, H. Pan, X. Lu, L. Gu, Y. S. Hu, H. Li, M. Armand, Y. Ikuhara, L. Chen and X. Huang, *Nat. Commun.*, 2013, **4**, 1870.
24 J. Liu, K. Tang, K. Song, P. A. van Aken, Y. Yu and J. Maier, *Phys. Chem. Chem. Phys.*, 2013, **15**, 20813.
25 K. T. Kim, G. Ali, K. Y. Chung, C. S. Yoon, H. Yashiro, Y. K. Sun, J. Lu, K. Amine and S. T. Myung, *Nano Lett.*, 2014, **14**, 416.
26 X. Yu, H. Pan, W. Wan, C. Ma, J. Bai, Q. Meng, S. N. Ehrlich, Y. S. Hu and X. Q. Yang, *Nano Lett.*, 2013, **13**, 4721.
27 Y. Xu, E. M. Lotfabad, H. Wang, B. Farbod, Z. Xu, A. Kohandehghan and D. Mitlin, *Chem. Commun.*, 2013, **49**, 8973.
28 Z. Q. Zhu, S. W. Wang, J. Du, Q. Jin, T. R. Zhang, F. Y. Cheng and J. Chen, *Nano Lett.*, 2014, **14**, 153.
29 Z. H. Zhou, Y. F. Deng, Y. Q. Jiang, H. L. Wan and S. W. Ng, *Dalton Trans.*, 2003, 2636.
30 Y. Shen, J. R. Eltzholtz and B. B. Iversen, *Chem. Mater.*, 2013, **25**, 5023.
31 Y. Qu, W. Zhou, Y. Xie, L. Jiang, J. Wang, G. Tian, Z. Ren, C. Tian and H. Fu, *Chem. Commun.*, 2013, **49**, 8510.
32 A. C. Ferrari and J. Robertson, *Phys. Rev. B: Condens. Matter Mater. Phys.*, 2000, **61**, 14095.
33 L. Fu, K. Tang, K. Song, P. A. van Aken, Y. Yu and J. Maier, *Nanoscale*, 2014, **6**, 1384.
34 L. Wu, D. Buchholz, D. Bresser, L. Gomes Chagas and S. Passerini, *J. Power Sources*, 2014, **251**, 379.
35 A. Rudola, K. Saravanan, C. W. Mason and P. Balaya, *J. Mater. Chem. A*, 2013, **1**, 2653.
36 T. Y. Ma, S. Dai, M. Jaroniec and S. Z. Qiao, *J. Am. Chem. Soc.*, 2014, **136**, 13925.
37 T. Chen, L. Pan, T. Lu, C. Fu, D. H. C. Chua and Z. Sun, *J. Mater. Chem. A*, 2014, **2**, 1263.
38 S. H. Ng, J. Wang, D. Wexler, K. Konstantinov, Z. P. Guo and H. K. Liu, *Angew. Chem., Int. Ed.*, 2006, **45**, 6896.

